

CMOS Tunable-Wavelength Multi-Color Photogate Sensor

Derek Ho, *Student Member, IEEE*, M. Omair Noor, Ulrich J. Krull, Glenn Gulak, *Senior Member, IEEE*, and Roman Genov, *Senior Member, IEEE*

Abstract—A CMOS tunable-wavelength multi-color photogate (CPG) sensor is presented. Sensing of a small set of well-separated wavelengths (e.g., >50 nm apart) is achieved by tuning the spectral response of the device with a bias voltage. The CPG employs the polysilicon gate as an optical filter, which eliminates the need for an external color filter. A prototype has been fabricated in a standard 0.35 μm digital CMOS technology and demonstrates intensity measurements of blue (450 nm), green (520 nm), and red (620 nm) illumination with peak signal-to-noise ratios (SNRs) of 34.7 dB, 29.2 dB, and 34.8 dB, respectively. The prototype is applied to fluorescence detection of green-emitting quantum dots (gQDs) and red-emitting quantum dots (rQDs). It spectrally differentiates among multiple emission bands, effectively implementing on-chip emission filtering. The prototype demonstrates single-color measurements of gQD and rQD concentrations to a detection limit of 24 nM, and multi-color measurements of solutions containing both colors of QDs to a detection limit of 90 nM and 120 nM of gQD and rQD, respectively.

Index Terms—CMOS image sensor, contact imaging, fluorescence, microsystem, quantum dots, spectral-multiplexing.

I. INTRODUCTION

FLUORESCENCE-BASED transduction is a mature technology and finds a multitude of applications in the life sciences. For many analytes, it provides the highest sensitivity and selectivity amongst common transduction methods [1]. In particular, laser-induced fluorescence is a prominent sensory method for lab-on-a-chip devices [2]. Several groups have focused on the development of integrated fluorescence-based sensing platforms for applications ranging from cancer research [3], [4] to nucleic acid detection [1], [5].

Conventional array based fluorescence sensing technologies, such as DNA microarrays [6], rely on spatial registration of probes to achieve space-multiplexed detection of target analytes. This requires additional steps for the preparation of surface chemistry which is prone to spatial variation. One of the

Manuscript received June 25, 2012; revised November 02, 2012; accepted December 13, 2012. This paper was recommended by Associate Editor T. Delbruck.

D. Ho, G. Gulak, and R. Genov are with the Department of Electrical and Computer Engineering, University of Toronto, Toronto, ON M5S 3G4, Canada (e-mail: roman@eecg.utoronto.ca).

M. O. Noor and U. J. Krull are with the Department of Chemical and Physical Sciences, University of Toronto Mississauga, Mississauga, ON L5L 1C6, Canada.

Color versions of one or more of the figures in this paper are available online at <http://ieeexplore.ieee.org>.

Digital Object Identifier 10.1109/TBCAS.2013.2243727

advantages of fluorescence-based sensing is its suitability for spectral multiplexing, which can be exploited to eliminate the need for spatial registration. To concurrently analyze multiple target analytes without spatial registration, different target analytes can be associated with different fluorescent markers that can be distinguished by their emission wavelengths. By measuring the emission intensity at each of these wavelengths, different targets, such as nucleic acid targets, can be simultaneously quantified [7].

Fluorescent markers, such as the green-emitting and red-emitting quantum dots (QDs) [8], absorb light and emit at a longer wavelength. Emission wavelengths are typically between 500 nm to 700 nm and well-separated (e.g., >50 nm apart). Therefore, unlike other spectroscopic applications where continuous fine resolution spectroscopy techniques (e.g., Raman spectroscopy) are required, fluorescence imaging requires the detector to provide spectral differentiation among only a small number of discrete wavelengths. Limits of detection in the range of nano- to micro-molars in a nano- to micro-liter sample volume have been reported for fluorescence sensing microsystems using custom optics such as waveguides and gratings in the last decade [9], [10]. Fluorescence emission light intensity has been increasing due to improvements in the quantum efficiency of fluorophores [10], [11]. Fluorescence detection is typically performed at room temperature (i.e., $\approx 25^\circ\text{C}$) [10].

Conventionally, differentiation between fluorescence emission wavelengths has been achieved by using a set of optical bandpass filters to select different parts of the emission spectrum [14] and subsequently sensing using a monochromatic photodetector. The optics involved is bulky and expensive. To circumvent this problem, filterless spectral sensing methods have also been investigated. Methods based on diffraction grating (the splitting of light) [15] and Fabry-Perot etalon (tuned resonance cavity) [16] generally offer high spectral resolution, but require micromachining and post-processing such as wafer polishing and wafer bonding. Eliminating the need for sophisticated optics and post-processing is the ultimate remedy to high design complexity and fabrication cost.

Techniques that solely rely on integrated circuit process technology have been developed, most notably buried junction technology [12], [17]–[22], on which the Foveon sensor is based, as shown in Fig. 1(a). Since light absorption in a semiconductor varies across wavelengths in such a way that light of a longer wavelength can penetrate deeper, a photocurrent measured at a deeper depth consists of stronger longer-wavelength components. By sensing at several depths, color information can be

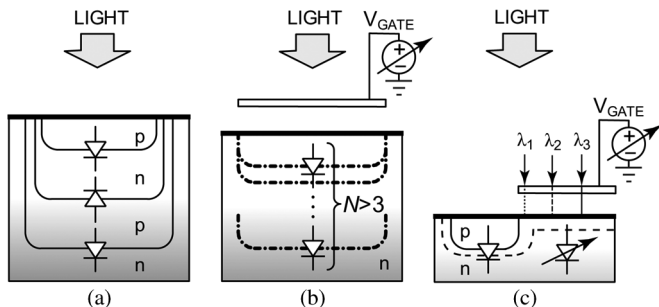


Fig. 1. Filterless integrated circuit spectral sensing approaches. (a) Buried triple $p - n$ -junction embedding diodes at three fixed depths [12]. (b) Photo sensing region depth modulation enabling light collection at multiple electronically-tunable depths in custom CMOS [13]. (c) Proposed standard-CMOS tunable-wavelength multi-color photogate consisting two sensing regions, one of which is tunable by a voltage bias and covered by a poly-Si gate.

inferred. Although the buried junction approach achieves high spatial density and is suitable for photographic applications requiring only three colors (e.g., blue, green, and red), there is a limit to the number of diodes that can be implemented, for example three for a dual-well process. This renders it unsuitable for applications that require sensing more than three wavelengths. To overcome this limitation, a spectrally-sensitive photodiode that can potentially sense more than three colors has been developed [23], as shown in Fig. 1(b). A biased poly-silicon gate modulates the photo sensing region depth to effectively achieve an equivalent of many buried $p - n$ -junctions. However, the reliance on the vertical dimensions of the CMOS process technology limits the scalability of the device dimensions. The most recently reported prototype is fabricated in a $5 \mu\text{m}$ custom process [23].

The choices of the photodetector for conventional fluorescence imaging systems have commonly been the photo multiplier tube (PMT) and the charge-coupled device (CCD). PMTs are amongst the most sensitive photodetectors, but are bulky, expensive and require a high operating voltage, making them unattractive to be integrated into a miniaturized system. The throughput of PMT-based detection systems is relatively low due to the lack of parallelism. CCDs can be employed in an arrayed implementation, but do not allow for the on-chip integration of peripheral circuits such as signal conditioning circuits. This increases cost and limits miniaturization. CMOS technology, on the other hand, has the advantages of low cost, high integration density, and signal processing versatility. Numerous recent designs based on the CMOS $p - n$ -junction photodiode have been reported including a time-resolved fluorescence imager [24] and a lab-on-chip fluorometer [25]. The monochromatic photogate structure typically used in a CCD has been demonstrated in CMOS [26]. However, the exploitation of the polysilicon gate to perform color sensing has largely been unexplored.

In this paper, we present a single-pixel tunable-wavelength multi-color photogate (CPG) sensor implemented in a standard digital $0.35 \mu\text{m}$ CMOS technology, validated in spectrally-multiplexed fluorescence contact sensing. Sensing of a small set of well-separated wavelengths (e.g., $>50 \text{ nm}$ apart) is based on tuning the spectral response of the CPG structure, as shown in

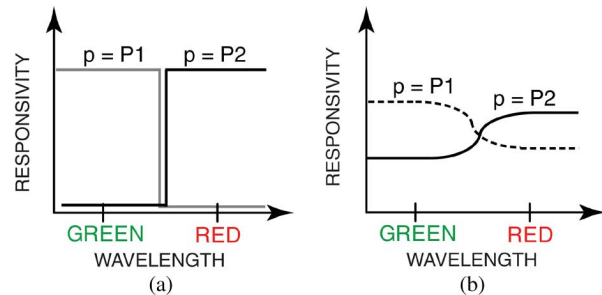


Fig. 2. The concept of tuning detector spectral responsivity with a control parameter for (a) an ideal device, and (b) a non-ideal device.

Fig. 1(c). The structure consists of two sensing regions, one of which can be modulated by a voltage bias to modify the overall CPG spectral response. The CPG has a structural resemblance to the conventional CMOS monochromatic photogate [26] but it employs the polysilicon gate as an optical filter, thus requiring no external optical color (i.e., band-pass) filters. The CPG is designed to sense light intensity of multiple wavelengths which are known *a priori*, hence, it is suitable for coarse color differentiation in multi-color fluorescence applications as the fluorescence emission colors are known before detection. The overall integrated sensor consists of the CMOS tunable color photogate, an on-chip analog-to-digital converter (ADC), and a software algorithm to reconstruct the input light intensities at specific wavelengths. The CPG has been validated in quantum dot fluorescence measurements where only one long-pass optical filter to attenuate the excitation light (but not to distinguish among emission light colors) is required. Preliminary results of the CPG have been reported in [27].

The rest of the paper is organized as follows. Section II discusses the conceptual model of the CPG sensor. Section III details the principle of operation. Sections IV and V report experimental results in light-emitting diode (LED) light measurements and QD fluorescence measurements, respectively. Section VI highlights key observations.

II. CONCEPTUAL MODEL

The tunable-wavelength multi-color photogate sensor measures the intensities of a small set of well-separated wavelengths (e.g., $>50 \text{ nm}$ apart). The principle of operation is first illustrated by an example and is subsequently formulated analytically.

A. Concept of Tunable Spectral Responsivity

Unlike the buried junction approach [12] that employs multiple discrete photodiodes, the CPG creates the equivalent of multiple photodetectors by tuning the spectral responsivity of a single detector through modulating a control parameter, p , which can be implemented as a bias voltage.

To illustrate, Fig. 2(a) presents a device whose response to p is ideal, for two colors. For example, to sense the green color, a measurement can be performed by setting the control parameter p to P1. Similarly, to sense the red color, the control parameter p is set to P2.

In practice, a device response may resemble that depicted in Fig. 2(b), where the device is sensitive to more than one color

for any value of p . Hence, the device output current contains a mixture of color components. In this case, one method to determine the intensity at each wavelength is by analyzing multiple measurements, each using a unique value of p , then solving for the input intensity for each color. For example, to sense the intensities at the green and red wavelengths, two measurements are required with the control parameter set to values P1 and P2. As illustrated in Fig. 2(b), each measurement is a linear combination of scaled color intensities. Also, the change in the device response with respect to p can be small, which is the key reason why in practice the device is restricted to the sensing of several well-separated wavelengths.

There are three types of variables involved: the detector responsivity to a particular wavelength, the measured photocurrent, and the input light intensity. A model of detector responsivity can be generated a priori, for example by measurement with known inputs. The input light intensity can then be calculated based on the set of measured photocurrents and the stored model.

B. Analytical Formulation

The above concept can be formulated analytically as follows. When the CPG is illuminated, the absorption of light is described by the Beer-Lambert law [28]. The absorbed photons generate electron-hole pairs, giving rise to a photocurrent for a single wavelength input that is given by

$$I = \frac{qS\lambda}{hc} \left(1 - e^{-\alpha(\lambda)D(p)}\right) A'(\lambda)\phi \quad (1)$$

where ϕ is the radiation intensity, q is the elementary charge, S is the area of the detector, λ is the wavelength, h is Planck's constant, c is the speed of light in vacuum, α is the absorption coefficient, D is the effective depth of the sensing region, and $A'(\lambda)$ is the absorption of a polysilicon gate structure. The absorption coefficient α is a function of λ . The aforementioned control parameter p determines the value of D . For a given detector size, (1) can be rewritten as

$$I = k(p, \lambda)\phi \quad (2)$$

where $k(p, \lambda)$ is the responsivity of the CPG and can be obtained empirically.

When light rays of multiple wavelengths are incident simultaneously, the photocurrent can be expressed as a linear combination of the CPG response at each wavelength. To determine the light intensities at each wavelength, multiple measurements are required. For example, for a two-wavelength input, the photocurrents I_1 and I_2 measured by the photodetector can be related to the input intensities ϕ_1 and ϕ_2 (at λ_1 and λ_2 , respectively) by

$$I_1 = k_{11}\phi_1 + k_{12}\phi_2 \quad (3)$$

$$I_2 = k_{21}\phi_1 + k_{22}\phi_2 \quad (4)$$

where the k -coefficients are such that k_{ij} is the detector responsivity under i -th control parameter to the j -th wavelength for $i = 1, 2$, and $j = 1, 2$. The input intensities ϕ_1 and ϕ_2 can be obtained by solving the system of equations, provided that

the detectors have unique spectral responses (i.e., (3) and (4) are linearly independent). This model can be extended to a finite set of N wavelengths. To determine the incident light intensity of an input spectrum to a resolution of N distinct wavelengths, N measurements are required, each with a different control parameter. Equations (3) and (4) thus extend to the N -variable system of equations

$$\begin{bmatrix} I_1 \\ I_2 \\ \vdots \\ I_N \end{bmatrix} = \begin{bmatrix} k_{11} & k_{12} & \cdots & k_{1N} \\ k_{21} & k_{22} & \cdots & k_{2N} \\ \vdots & \vdots & \ddots & \vdots \\ k_{N1} & k_{N2} & \cdots & k_{NN} \end{bmatrix} \begin{bmatrix} \phi_1 \\ \phi_2 \\ \vdots \\ \phi_N \end{bmatrix}. \quad (5)$$

To empirically construct a $N \times N$ k -matrix model depicted in the system of (5), each k -coefficient is obtained by measuring the CPG photocurrent using a known illumination and the corresponding control parameter. For example, k_{11} is obtained by inputting ϕ_1 (a known intensity at wavelength 1) and measuring the CPG photocurrent under the control parameter p_1 . Analogously, k_{12} is obtained from ϕ_2 and p_1 , and k_{21} is obtained from ϕ_1 and p_2 . This process is repeated $N \times N$ times to build the entire k -matrix. This computation is only performed once so this computation load is minimal. The model of (5) is then used to solve for the N unknown light intensities ϕ based on N measured currents I .

Provided that the wavelengths are well-separated, this method offers the flexibility to tune to an arbitrary set of wavelengths within the sensitivity range of the silicon photodiode. However, one limitation of this approach is that it requires the complete set of sensor input wavelengths be known *a priori* so that the appropriate k -coefficient model can be developed. As counterexamples, the sensor would report incorrect intensities if the input wavelengths differ from that of the model used in reconstruction, or if three wavelengths are present at the input but only a two-wavelength model is used.

III. PRINCIPLE OF OPERATION

A. Qualitative Analysis

In polysilicon, light is absorbed exponentially as a function of penetration depth [28]. Optical transmittance T , the portion of light that passes through a layer of polysilicon with thickness l can be approximated as

$$T_{gate} = e^{-\alpha(\lambda)l} \quad (6)$$

where $\alpha(\lambda)$ is the wavelength-dependent absorption coefficient, with values 3.56, 1.35, and 0.45 μm^{-1} for the wavelengths of 450 nm (blue), 520 nm (green), and 620 nm (red), respectively [28]. Fig. 3 depicts the optical transmittance of a polysilicon layer calculated based on the aforementioned absorption coefficients. For example, in the 0.35 μm CMOS process, the thickness of the polysilicon gate is approximately 300 nm [29], leading to an approximate transmittance of 35% for blue light (450 nm), 70% for green light (520 nm), and 85% for red light (620 nm). This property of the polysilicon MOS gate is utilized in the tunable color photogate design. It is worth noting that the gate is a well-fabricated structure in the CMOS process, with

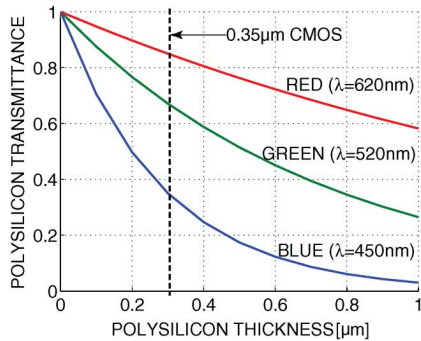


Fig. 3. Simulated wavelength-dependent optical transmittance of polysilicon.

an intra-die thickness variation on the order of 3% [30]. The resulting variation of the optical transmittance can be observed in Fig. 3.

The tunable color photogate is schematically depicted in Fig. 4(a), structurally resembling the conventional surface-channel monochromatic CMOS photogate [26]. The core sensing region of the CPG is the large area covered by the polysilicon gate. A small p^+ -diffusion, referred to as the edge region, forms the device output. A n^+ -diffusion fabricated in an n -type body forms the an ohmic bias contact. The p^+ -output diffusion is set by the readout circuit to a voltage lower than the n -body voltage to maintain a reverse biased $p - n$ -junction.

The gate performs two key functions for color sensing. First, it functions as an optical filter to provide wavelength-dependent absorption as described above. Second, it is a terminal for the induction of an electric field to modulate the photo-generated carrier collection efficiency in the core region, the area under the gate. The gate-to-body biasing voltage V_{GB} acts as the control parameter, p . When V_{GB} is applied such that no depletion region is formed under the gate, as depicted in Fig. 4(a) cases A and B, photo detection only takes place near the p^+/n -body depletion region. As depicted in Fig. 4(a) cases C through E, when another V_{GB} is applied to form a depletion region at the CPG core, it also participates in photo detection. But the light experiences wavelength-dependent absorption as it travels through the gate. Since the gate provides greater attenuation at shorter wavelengths, the core region provides additional long-wavelength (e.g., red) responsivity to the CPG. Since the edge and core of the CPG have different spectral properties, when different gate voltages are applied, an equivalent of multiple detectors with unique spectral responses is created, e.g., for two colors, (3) and (4) are implemented by a single device.

The formation of the depletion region is for the purpose of modulating the carrier collection efficiency rather than depth-based color sensing. To understand the formation of the depletion region at the device core, the respective energy profiles of the CPG are depicted in Fig. 4(b). Depicted energy levels are the gate Fermi level E_{Fm} , semiconductor Fermi level E_{Fs} , intrinsic semiconductor Fermi level E_i , substrate conduction band E_C , and valence band E_V . As V_{GB} changes, the CPG transits through modes of operations, analogous to a metal-oxide-semiconductor (MOS) capacitor. This mode change leads to a change in carrier collection efficiency, which when functioning with the

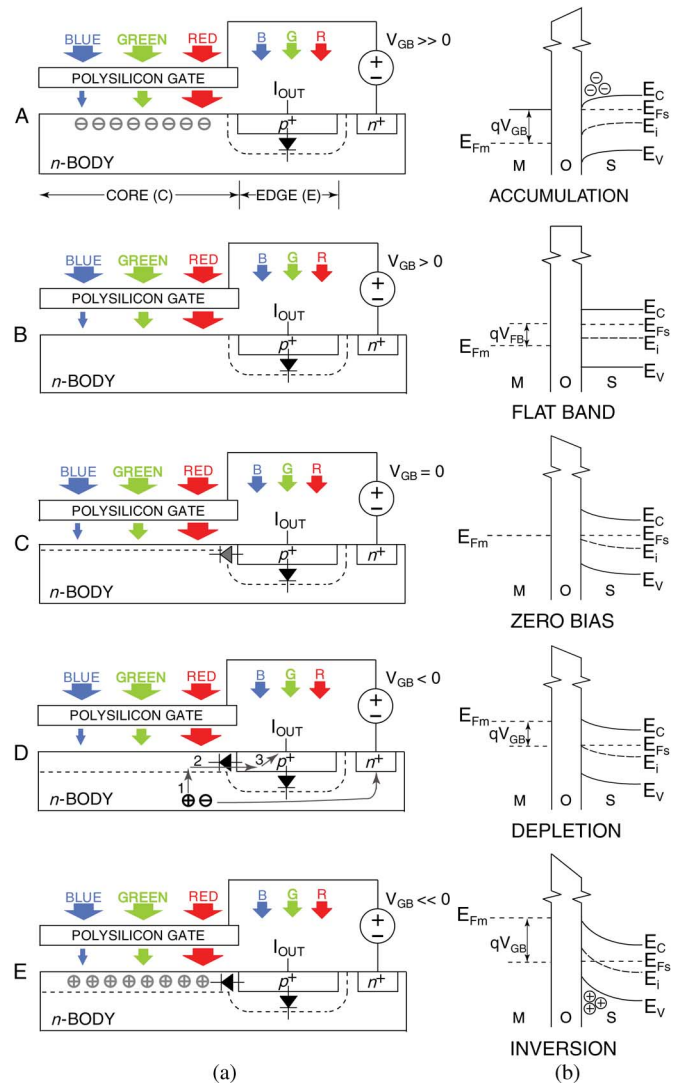


Fig. 4. CPG modes of operation are illustrated as various cases. (A) Accumulation. (B) Flat band. (C) Zero bias. (D) Depletion, with illustration of photo-generated carrier flow. (E) Inversion. (a) Cross-section diagram illustrating the location of carriers. (b) Energy band diagram illustrating the modes of operation of the CPG with a polysilicon gate and a n -doped body. Depicted are the gate Fermi level E_{Fm} , substrate conduction band E_C , semiconductor Fermi level E_{Fs} , intrinsic semiconductor Fermi level E_i , and valence band E_V . V_{GB} is the gate-to-body voltage.

wavelength-dependent absorption of the gate, leads to a change in device spectral properties.

Depicted in Fig. 4 case A, at a high gate-to-body bias, $V_{GB} \gg 0$, the electric field from the gate attracts electrons to the surface of the n -body. This is the accumulation mode. The high density of electrons in the surface layer of the n -body is exactly matched by the high density of holes at the gate, induced by the positive gate voltage applied. The appearance of extra electrons in the surface region of the substrate means that the Fermi level, E_{Fs} , in the surface region is close to the conduction band, E_C . The energy levels (E_C , E_i , and E_V) are, therefore, bent downwards going from the silicon substrate toward the gate. In this mode, the CPG core region is inactive. Photo detection only takes place in the p^+/n -body depletion region at the edge region of the device, hence producing a small photocurrent.

Depicted in Fig. 4 case B, as V_{GB} decreases, the CPG enters the flat band mode, where the electrons in the n -body are compensated by the positive donor ions and the minority holes. Due to the work function difference between the gate and the substrate, the Fermi levels of the gate, E_{Fm} , and the substrate, E_{Fs} , are different. This difference is related to the flat band voltage V_{FB} . Therefore, the flat band condition generally does not occur at zero bias [28]. The only depletion region is at the edge p^+/n -body junction. As V_{GB} reduces, passing the flat band biasing point, the CPG core begins to develop favorable potential for the collection of photo-generated carriers, which leads to a photocurrent contribution from the core.

Depicted in Fig. 4 case C, as V_{GB} reaches zero, the CPG enters the zero bias mode. The Fermi level is constant throughout the system due to thermal equilibrium. There is a potential difference between the gate and the n -body at zero bias. This is analogous to the built-in voltage in $p-n$ -junctions [28]. In this mode, a shallow depletion region is formed in the core region since the biasing condition deviates from that required for the flat band condition.

Depicted in Fig. 4 case D, when a small voltage $V_{GB} < 0$ is applied, the electric field produced repels the electrons from the surface of the silicon substrate, creating a depletion layer. The CPG core is thoroughly depleted at this surface when the n -body intrinsic Fermi level E_i equals E_{Fs} there. The thoroughly depleted CPG has a well-developed depletion region and associated electric field to collect photo-generated carriers, therefore the photocurrent reaches a high level.

Depicted in Fig. 4 case E, when $V_{GB} \ll 0$, the CPG enters the strong inversion mode. As the energy difference between the valence-band E_V and the substrate Fermi level E_{Fs} is reduced, holes begin to appear at the surface of the substrate. However, these additional holes do not participate in photo-sensing, which results in a relatively high photocurrent, approximately constant across both the depletion and strong inversion modes.

The CPG in both the depletion mode and inversion mode has a well-developed depletion region to collect carriers as depicted in Fig. 4 cases D and E. Fig. 4 case D depicts the flow of photo-induced charge carriers within the CPG. Due to the photo-electric effect, when light of sufficient energy breaks a bond, creating an electron-hole pair, carriers travel via several different mechanisms as follows: (1) minority carrier holes in n -body travel to depletion region via diffusion formed by a carrier concentration gradient; this gradient is formed by the fact that the depletion region is deprived of carriers; (2) holes in the depletion region travel to p^+ -output diffusion via drift induced by the electric field resulting from the space charges of the p^+/n -body junction, and (3) majority carrier holes in p^+ -output diffusion travel to the output electrode by drift due to the (low) potential at the electrode. Photo-generated electrons drift to the n^+ ohmic contact due to its (high) applied potential and are discharged, i.e., not collected as a part of the photocurrent.

B. Quantitative Analysis

Given that the electric field in the depletion layer immediately separates the photo-generated electrons and holes, an expression

can be written for the photocurrent based on the external generation rate G_{ext} . The external generation rate, in contrast to generation due to thermal mechanisms, is the number of electron-hole pairs generated in a unit of the depletion-layer volume per second. The photocurrent of a $p-n$ -junction photodiode is given by [28]

$$I_{ph} = qG_{ext}A_jD_j \quad (7)$$

where q is the elementary charge, A_j is the $p-n$ -junction area (where the depletion layer is formed), and D_j is the depletion region depth. Since uniform carrier generation in the sensing volume and complete carrier collection are assumed, D_j is an approximated value. The external generation rate G_{ext} can be related to the incoming optical input as

$$G_{ext} = \frac{P_{d,in}R(\lambda)}{q} \quad (8)$$

where $P_{d,in}$ is the input optical power density, in the units of $W/\mu m^3$, and $R(\lambda)$ is the responsivity of the detector, in A/W , which is wavelength-dependent.

Since the CPG has both the core region and the edge region, its photocurrent can be modeled as the sum of photocurrents in these regions. The photocurrent of the core region, $I_{ph,core}$, which is V_{GB} -dependent, is given by

$$I_{ph,core}(V_{GB}) = P_{d,in}T_{gate}R_{core}(\lambda)A_{core}D_{core}(V_{GB}) \quad (9)$$

where T_{gate} is the transmittance of the polysilicon gate, $R_{core}(\lambda)$ is the responsivity of the core region, A_{core} is the core area, and $D_{core}(V_{GB})$ is the core sensing depth, which is dependent on V_{GB} . T_{gate} is utilized to model the attenuation of the input light by the polysilicon gate.

Analogously, the photocurrent of the edge region, $I_{ph,edge}$ is given by

$$I_{ph,edge} = P_{d,in}R_{edge}(\lambda)A_{edge}D_{edge} \quad (10)$$

where $R_{edge}(\lambda)$, A_{edge} , and D_{edge} are the responsivity, area, and depth of the edge sensing region, respectively.

To gain insight into $D_{core}(V_{GB})$, next, the relationship between depletion depth and V_{GB} is formulated based on three regimes. For $V_{GB} > V_{FB}$, where V_{FB} is the flat band voltage, there is no depletion in the CPG core

$$D_{core} = 0 \quad (V_{GB} > V_{FB}). \quad (11)$$

For $V_{INV} < V_{GB} < V_{FB}$, where V_{INV} is the voltage that triggers the onset of inversion, the depletion depth grows with decreasing V_{GB} until inversion is reached. The depletion depth is given by [28]

$$D_{core} = \sqrt{\frac{2\epsilon_s V_{GB}}{qN_d}} \quad (V_{GB} > V_{FB}) \quad (12)$$

where $\epsilon_s = 1.03 \times 10^{14}$ F/m is the permittivity of silicon and N_d is the donor concentration in the n -type body.

For $V_{GB} < V_{INV}$, it is assumed that further reduction in V_{GB} results in stronger inversion rather than in more depletion. Thus, the maximum value of the depletion depth is reached

$$D_{core} = D_{MAX} \quad (V_{GB} < V_{INV}). \quad (13)$$

Strong inversion is achieved when the semiconductor surface contains a density of holes equivalent to that of electrons in the body, i.e., it is as strongly p -type as the body is n -type. Under this condition, V_{MAX} , the voltage with respect to V_{FB} required to induce D_{MAX} , is given by [28]

$$V_{MAX} = 2 \frac{kT}{q} \ln \frac{N_d}{n_i} \quad (14)$$

where k is Boltzmann's constant, T is absolute temperature (at $T = 298^\circ\text{K}$, $kT/q \approx 25$ mV), and n_i is the intrinsic carrier concentration ($\approx 10^{10} \text{ cm}^{-3}$ at $T = 298^\circ\text{K}$). Therefore, D_{MAX} is given by substituting V_{INV} for V_{GB} into (12)

$$D_{MAX} = \sqrt{\frac{2\epsilon_s V_{MAX}}{qN_d}} = 2 \sqrt{\frac{\epsilon_s kT \ln \left(\frac{N_d}{n_i} \right)}{q^2 N_d}}. \quad (15)$$

With expressions for the depletion depth under different V_{GB} ranges, the total photocurrent of the CPG is readily obtained by the summation of the current components at the core and edge regions

$$I_{ph,cpg}(V_{GB}) = I_{ph,core}(V_{GB}) + I_{ph,edge}. \quad (16)$$

It is interesting to note that for $V_{GB} > V_{FB}$, since $D_{core} = 0$ which leads to $I_{ph,core}(V_{GB}) = 0$, the above formulation correctly describes the fact that the CPG photocurrent comes solely from the edge region.

Fig. 5 depicts the approximate theoretical photocurrent for a $50 \mu\text{m} \times 50 \mu\text{m}$ CPG across V_{GB} for $V_{BODY} = 1.5$ V, under $1.7 \text{ pW}/\mu\text{m}^2$ of 620 nm (red) optical illumination. The photocurrent is obtained based on (7)–(16). As V_{GB} reduces, the CPG transitions through various modes of operation, in order, accumulation (A), flat band (B), zero bias (C), depletion (D), and inversion (E). For the typical n -body doping level of $1 \times 10^{16} \text{ cm}^{-3}$ [28], the value of V_{FB} is approximately 0.45 V and $V_{MAX} = 0.71$ V (from (14)). Therefore, the flat band condition is reached at $V_{GB} \approx 0.45$ V. Beyond this point, the core depletion depth D_{core} starts increasing [according to (12)] as V_{GB} increases. This lasts for 0.71 V to the final value of $D_{MAX} = 0.41 \mu\text{m}$ [from (15)] at which point inversion is reached. Once the depletion region fully forms, the core provides a substantial component to the overall CPG photocurrent. Although the change in the depletion region depth contributes to wavelength-dependent sensing, this effect does not appear to be significant as can be observed in subsequent experimental results. This depth change is primarily responsible for modulating the photo-generated carrier collection efficiency, after light experience wavelength-dependent absorption in the poly gate. The value for D_{edge} of $1 \mu\text{m}$ for a typical $0.35 \mu\text{m}$ process is used [31]. Since it is assumed that approximately 40% of incoming light is attenuated by the various oxide layers over the entire chip, the value of 0.3 A/W for R_{core} and R_{edge} in (9) and (10) is used, which corresponds to a 60% quantum

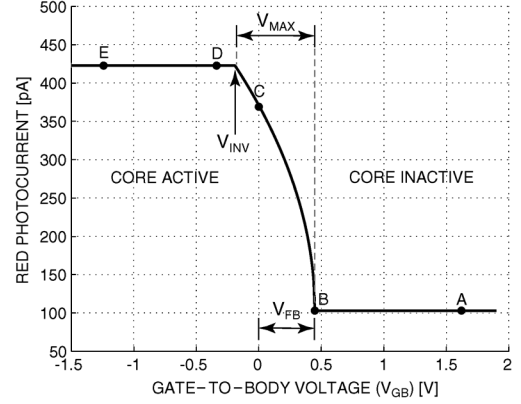


Fig. 5. Theoretical (first-order approximated) CPG photocurrent versus gate-to-body voltage under 620 nm (red) illumination for a $50 \mu\text{m} \times 50 \mu\text{m}$ device and a body bias of 1.5 V.

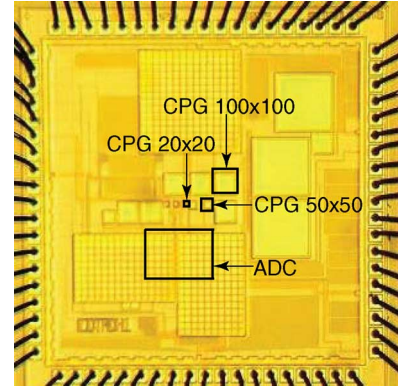


Fig. 6. $2 \text{ mm} \times 2 \text{ mm}$ die micrograph of the fabricated $0.35 \mu\text{m}$ standard CMOS test chip.

efficiency. With $T_{gate}(\lambda = 620 \text{ nm}) = 0.85$ (from Fig. 3), $A_{core} = 48 \mu\text{m} \times 48 \mu\text{m}$, $A_{edge} \approx 50 \mu\text{m} \times 1 \mu\text{m} \times 4$, the CPG photocurrent is calculated using equation (16) to be 102 pA and 418 pA when the core is active and inactive, respectively.

IV. VLSI IMPLEMENTATION

The CPG has been prototyped in a $0.35 \mu\text{m}$ standard CMOS technology as depicted in Fig. 6. The fabricated CPG cross-sectional view is illustrated in Fig. 7, with p^+ and n^+ diffusion regions implemented as concentric ring structures. The entire CPG is fabricated in an n -body for isolation of substrate noise and crosstalk from adjacent pixels in an arrayed implementation.

The sensor integrates an on-chip current-to-frequency ADC. The ADC consists of a comparator and a digital counter. The comparator has one input connected to the CPG and the other to a reference voltage. Photocurrent from the CPG is integrated onto its parasitic capacitor, building the voltage across it. If this voltage exceeds the reference voltage, the comparator triggers a reset operation and the photodiode voltage is reset to its dark value. The counter is incremented for every reset. Therefore, at the end of the exposure, the counter value is proportional to the light intensity. Results reported in Sections V and VI are obtained through this ADC.

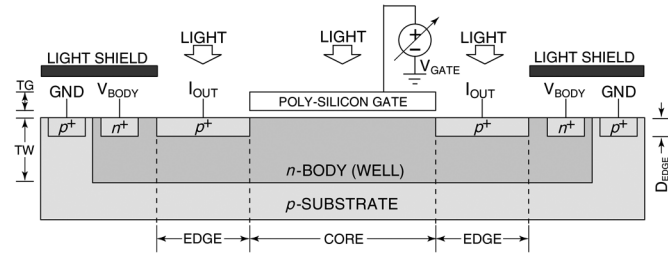


Fig. 7. Cross-section of the fabricated CMOS tunable-wavelength multi-color photogate (CPG) in 0.35 μm CMOS. Dimensions are $T_G \approx 0.3 \mu\text{m}$, $T_W \approx 1.5 \mu\text{m}$, and $D_{\text{edge}} \approx 1 \mu\text{m}$.

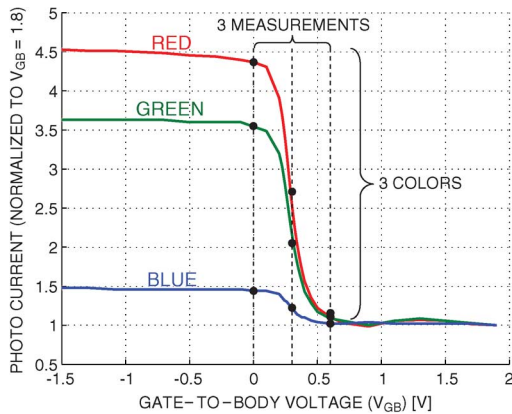


Fig. 8. Measured 50 $\mu\text{m} \times 50 \mu\text{m}$ CPG photocurrent for monochromatic light at 620 nm (red), 520 nm (green), and 450 nm (blue). $V_{\text{BODY}} = 1.5 \text{ V}$.

Fig. 8 depicts the measured photocurrent of a 50 $\mu\text{m} \times 50 \mu\text{m}$ CPG across gate voltages for blue (450 nm), green (520 nm), and red (620 nm) input illumination provided by LEDs, with full width at half maximum (FWHM) of 20 nm. For each color, approximately 3×10^{13} photons/sec/cm² were incident on the photodiode surface. Current measurements are obtained by a semiconductor parameter analyzer. To highlight the relative change in the current, the results are normalized to one at $V_{\text{GB}} = 1.8 \text{ V}$. As V_{GB} changes from a high voltage to a low voltage, the CPG core gradually becomes active, leading to increased photocurrent. As depicted in Fig. 8, the photocurrents across colors change to different extents. For a V_{GB} change from 1.8 V to -1.5 V ($V_{\text{BODY}} = 1.5 \text{ V}$), the increase in the photocurrent for blue, green, and red illuminations are 50%, 260%, and 350%, respectively. To a first-order approximation, these percentages are due to the absorption of light at specific wavelengths by the polysilicon gate as illustrated in Fig. 3, rather than due to a change in the core depletion region depth. The ability of the CPG to sense spectrally is based on this difference in the photocurrents which is the most prominent for V_{GB} between 0 and 0.6 V. Therefore, in order to resolve the input illumination at, for example, three wavelengths (i.e., three colors), V_{GB} of 0 V, 0.3 V, and 0.6 V are used for the three measurements required by (5).

The CPG can be characterized by its responsivity, the ratio of the photocurrent to the input illumination power, commonly expressed in the units of A/W. The responsivity is calculated by dividing the simulated CPG photocurrent by the illumination

power collected within the the total CPG area, including both the core and edge regions.

Fig. 9(a)–(c) depict measured and simulated CPG photocurrents for three device sizes: 20 $\mu\text{m} \times 20 \mu\text{m}$, 50 $\mu\text{m} \times 50 \mu\text{m}$, and 100 $\mu\text{m} \times 100 \mu\text{m}$. All devices have 1 μm edge regions. Both cases where the CPG core region is active (‘ON’) and inactive (‘OFF’) are depicted. Photocurrent simulations have been performed in the Crosslight optoelectronic simulator [32]. To highlight the relative change in the responsivity across wavelengths, Fig. 9(d)–(f) depict the ratio of the simulated ON-current to the OFF-current. The simulated structure is depicted in Fig. 7. Process parameters used, such as gate thickness (t_{GATE}) (0.3 μm), n -body doping (10^{16} cm^{-3}) and n -body depth (1.5 μm), are for a typical 0.35 μm standard CMOS process [29].

At short wavelengths, the photocurrent is low due to the gate absorption, which attenuates light before it reaches the sensing regions. At long wavelengths, light penetrates deeper into the substrate than the n -body depth, resulting in a reduction in the portion of carriers that can be collected.

The responsivity is low when the core is inactive as illumination power is lost to the core that does not generate any photocurrent. Comparing among the three CPG sizes using Fig. 9(a)–(c), unlike the photocurrent which is lower for a small device, the CPG responsivity is higher for a small device. A smaller device has a larger perimeter-to-area ratio, hence a proportionately larger edge region. This edge region is not covered by the light-attenuating gate, therefore it has a higher responsivity than the core region. The higher current output per unit area of a smaller device therefore leads to its higher responsivity.

The gate thickness is typically a fixed parameter for a process, but it is illustrative to analyze the associated tradeoff with responsivity and spectral selectivity. Fig. 10 depicts the effect of variation in the gate thickness (e.g., for a process design or due to process variation). Fig. 10(a) shows that the responsivity improves as t_{GATE} decreases, since more light can reach the sensing region without being absorbed by the gate.

Fig. 10(b) depicts the ratio R of the ON-current to the OFF-current, for the core being active and inactive, respectively. In order for the CPG to differentiate two wavelengths $\Delta\lambda$ nm apart, the change in the ON-OFF current ratio ΔR must be non-zero to ensure, for the two-color case, $k_{11}/k_{21} \neq k_{21}/k_{22}$ in (3) and (4). For example, if a change in V_{GB} merely affects responsivity to all wavelengths to the same extent, then R would be a constant across wavelengths, and measuring multiple times for different V_{GB} would not yield additional spectral information. The slope $m = \Delta R/\Delta\lambda$ is thus a representation of the spectral selectivity and is ideally large. It can be observed from Fig. 10(b) that m has a high value from 400 nm to 650 nm, which covers the emission spectra of most fluorescent biomarkers and the visible spectrum. Based on Fig. 10(a) and (b), a tradeoff can be observed where a thicker gate translates to better filtering which is essential for spectral selectivity, at the expense of reduced responsivity.

The effect of varying the area covered by the gate relative to the total device area on responsivity and spectral selectivity is shown in Fig. 11 for different core and edge dimensions, as defined in Fig. 7. Fig. 11(a) compares two 100 $\mu\text{m} \times 100 \mu\text{m}$ CPGs and shows that the responsivity improves as core area decreases,

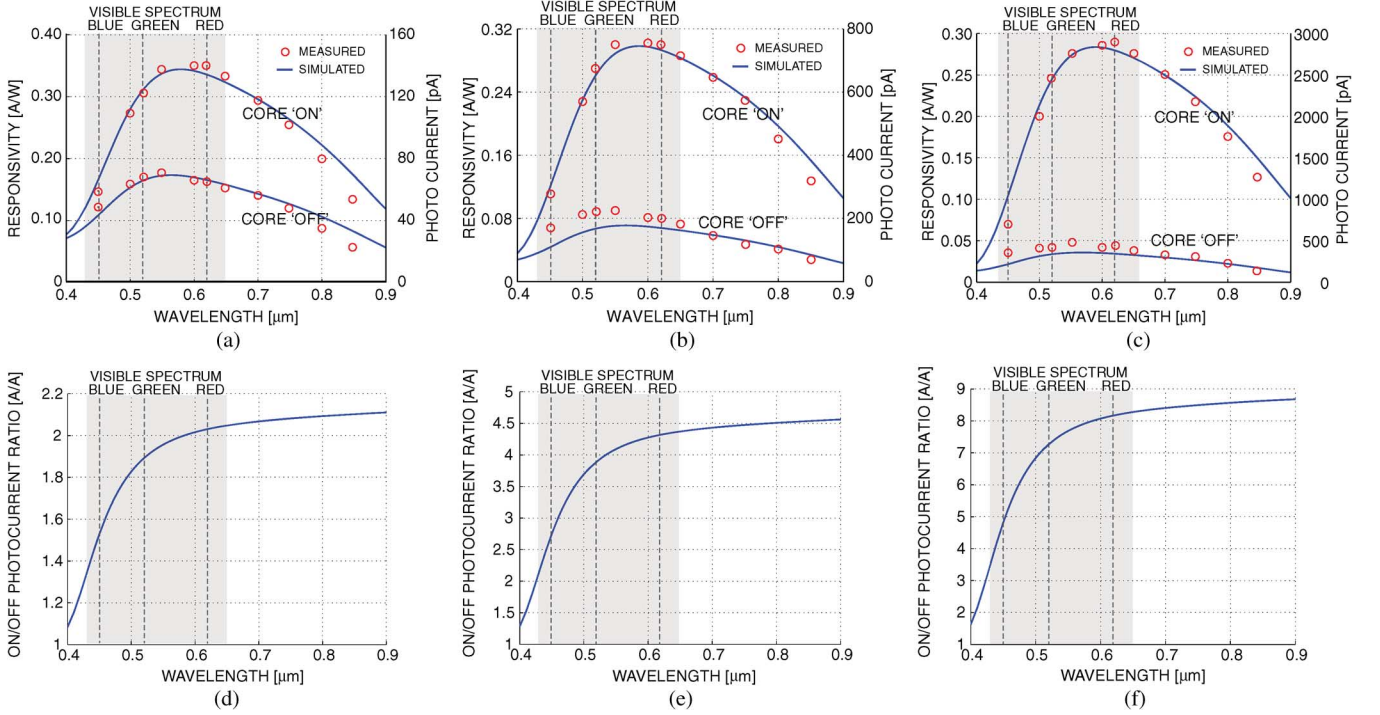


Fig. 9. Responsivity (experimentally measured results superimposed on simulated results) for different CPG device sizes. (a) $20 \mu\text{m} \times 20 \mu\text{m}$. (b) $50 \mu\text{m} \times 50 \mu\text{m}$. (c) $100 \mu\text{m} \times 100 \mu\text{m}$ device. B, G, and R denote blue, green, and red light, respectively. (d)–(f) are obtained from dividing the simulated ON-current by the OFF-current, highlighting the relative change in responsivity across wavelengths.

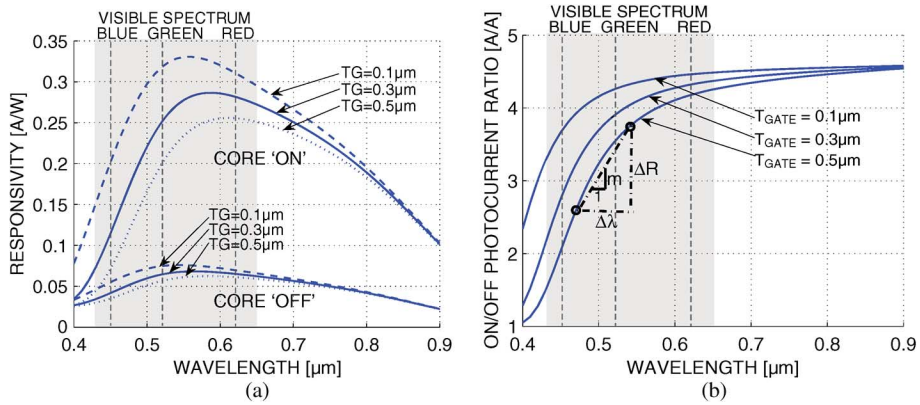


Fig. 10. Simulated (a) responsivity and (b) ON/OFF current ratio for $50 \mu\text{m} \times 50 \mu\text{m}$ CPG for three values of the gate thickness (t_{GATE}).

due to reduced light absorption by the gate. However, analogous to the aforementioned tradeoff, Fig. 11(b) shows that large gate coverage is essential to good spectral selectivity. In fact, a smaller device, Device III (CORE = $48 \mu\text{m}$, EDGE = $1 \mu\text{m}$), outperforms Device I (CORE = $50 \mu\text{m}$, EDGE = $25 \mu\text{m}$) in terms of maximizing the slope m , suggesting that the spectral selectivity is primarily sensitive to the ratio CORE/EDGE, instead of the absolute size of the CPG.

Given the above analysis, the way in which the CPG differs from conventional depth-based approaches to spectral sensing [12], [23] can be readily understood. The vertical dimension, such as diffusion depth or well depth, of depth-based devices [12], [23] is of intrinsic importance to their spectral performance since an appropriate absorption depth D is required to be able to sense a particular wavelength. But as CMOS devices scale to deep sub-micron planar dimensions, their vertical di-

mension is often $< 100 \text{ nm}$ [31], rendering the device only sensitive to very short (possibly non-visible) wavelengths. Whereas, although CPG operation involves the formation of the depletion region under the gate structure, its spectral responsivity is predominately due to the absorption property of the poly-silicon gate, a layer available in any standard CMOS technology requiring no additional cost or fabrication steps. Specifically, in Fig. 8, where the CPG core is fully active ($V_{\text{GB}} \ll 0 \text{ V}$), the normalized photocurrents of 1.5, 3.6, and 4.5 for the colors blue, green, and red, respectively, are largely due to the gate absorption and are not a result of sensing at precise depths. This makes the CPG be tolerant to device and technology scaling.

V. VALIDATION IN LED COLOR LIGHT MEASUREMENTS

The $0.35 \mu\text{m}$ prototype depicted in Fig. 6 has been tested in light intensity measurements at the blue (450 nm), green

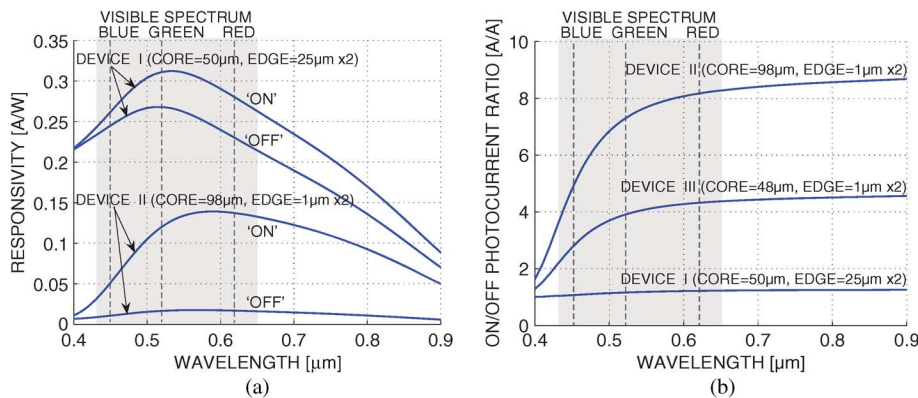


Fig. 11. Simulation results for CPGs with various values of core size and edge width. (a) Responsivity. (b) ON/OFF current ratio.

(520 nm), and red (620 nm) wavelengths using three current-controlled LEDs for input illumination. In order to measure the intensity at three known wavelengths, according to (5), an empirical model with nine k -coefficients is required. The extraction of k -coefficients can be performed as follows. For example, in (3), to extract k_{11} , a known ϕ_1 serves as the input of the measurement I_1 (at V_{GB1}). Similarly, for k_{12} , a known ϕ_2 is applied as input for another measurement at V_{GB1} . This process is then repeated across all wavelengths and gate voltages. Following the above procedure, only nine measurements are required to determine all nine k -coefficients. But it has been found that the modeling accuracy can be improved by simultaneously utilizing multiple combinations of input colored light intensities to solve for the average k -coefficients in (5). After the k -coefficients are obtained once, they are stored and reused for subsequent reconstruction calculations.

To resolve the input to three wavelengths, each input is measured three times using the discrete V_{GB} values of 0 V, 0.3 V and 0.6 V as shown in Fig. 8. The raw measurements and the previously obtained model are combined to reconstruct the input using (5). Fig. 12 depicts measured intensities after reconstruction for an illumination that simultaneously contains blue, green, and red light. Fig. 12(a)–(c) depict, respectively, measured blue, green, and red components of the input. For each of the three wavelengths, intensities at 0, 100, 500, 1000, and 1500 $\mu\text{W}/\text{cm}^2$ have been tested, which covers the entire emission intensity range of commonly used biomarkers. In order to evaluate the crosstalk between color channels, for each intensity step, the intensities of the other two colors are swept. For example, in Fig. 12(a), the blue intensity is held constant while green and red intensities are varied. This process is repeated five times across the blue intensity levels. Therefore, for the five intensity levels, each against 25 combinations of the other two colors, a total of 125 measurements have been performed. To highlight the reconstructed measured intensity variations, Fig. 12(d)–(f) are an alternative representation of Fig. 12(a)–(c), respectively. Each error bar contains the data from one plane and depicts one standard deviation from the mean value. The signal-to-noise ratio (SNR) is defined for imagers as $SNR = \mu/\sigma$, where μ and σ are mean and standard deviation of the output calculated over temporal measurements [33]. The peak SNRs as calculated at 1500 $\mu\text{W}/\text{cm}^2$ (limited by LED output power) are 34.7 dB, 29.2 dB, and 34.8 dB for the

blue, green, and red components, respectively. It is worth noting that the variation σ in theory contains both color crosstalk and temporal noise due to the pixel and ADC readout circuits. However, as can be observed in Fig. 12(a)–(c), the planes are relatively horizontal, indicating that the measurements of a particular color component have no significant dependency on the intensity of the other colors. The results suggest the variations are largely due to the temporal noise, which can be mitigated by multiple sampling and averaging. Table I summarizes key chip characteristics.

VI. VALIDATION IN COLOR FLUORESCENCE MEASUREMENTS

The CPG has been integrated into a microsystem, depicted in Fig. 13(a), for validation in the detection of green-emitting quantum dots (gQDs) and red-emitting quantum dots (rQDs). QDs are becoming well-adopted as they possess a number of unique optical properties that make them useful as fluorescent markers for spectral multiplexing. These properties include broad excitation spectra, greater resistance to photobleaching than organic fluorophores, larger attainable Stokes shifts (>100 nm) and size-tunable narrow and symmetrical emission spectra [8]. The QD absorption and emission spectra are depicted in Fig. 13(b). The CPG is used to spectrally differentiate the green and red fluorescence emissions, essentially performing on-chip emission filtering.

A. Fluorescence Contact Sensing Microsystem Setup

The microsystem, depicted in Fig. 13(a), consists of an LED for excitation, an optical emission filter, a fluidic structure, and the CPG sensor for photo detection. Excitation is provided by a 450 nm (FWHM = 20 nm) LED, the blue channel of the Luxeon K2 LED system [34] used in the LED color light measurements. The excitation light is directed through the optical filter to attenuate the excitation light intensity. A thin-film optical interference filter is chosen for this microsystem. It has been tested in laboratory conditions to provide an optical density of six (i.e., factor of 10^6) excitation light attenuation. The performance of the thin-film filter reduces as scattered light rays deviate from the ideal perpendicular-to-the-surface angle of incidence by more than 20 degrees. This behavior is characteristic of interference filters.

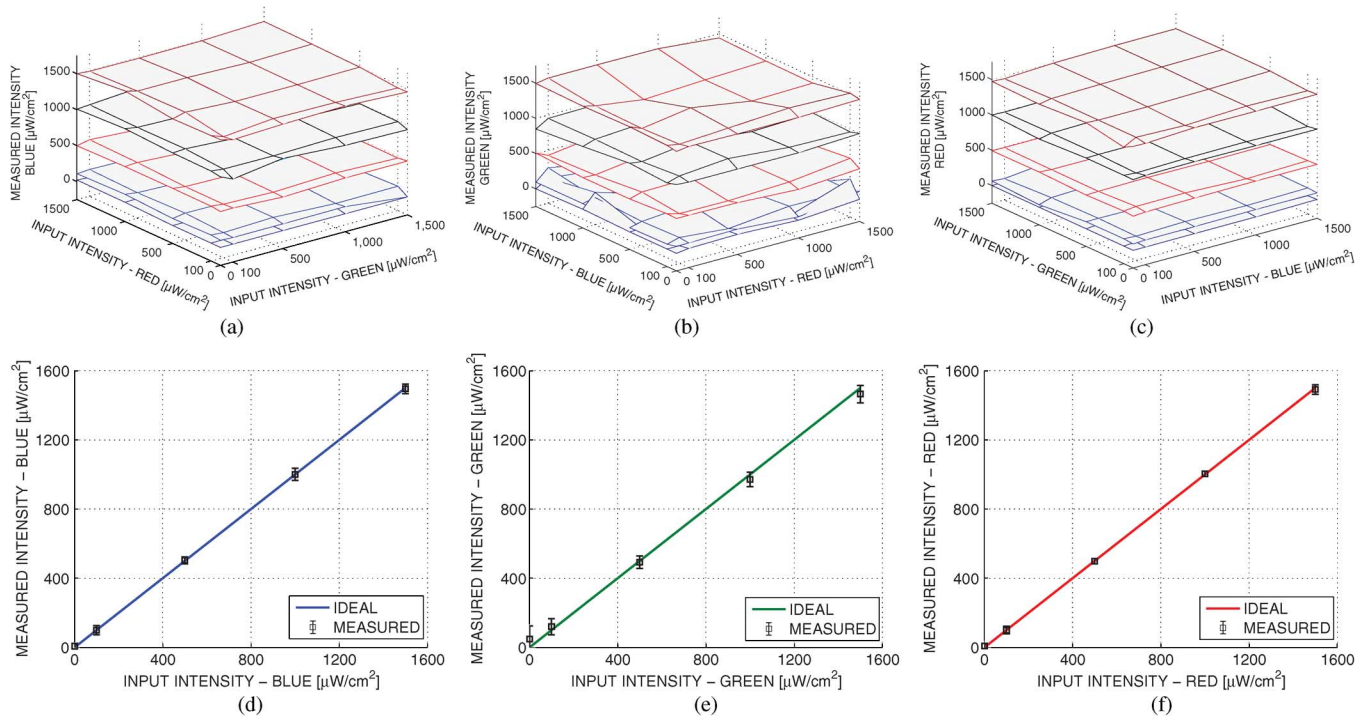


Fig. 12. Simultaneous three-color LED illumination measurements. (a)–(c) Reconstructed intensity of the blue (450 nm), green (520 nm) and red (620 nm) input components, respectively. (d)–(f) Alternative visualization of (a)–(c), respectively, one error bar (1σ) per plane.

TABLE I
CHIP CHARACTERISTICS

Technology	0.35 μm standard CMOS
Supply Voltage	3.3V
CPG Sizes	20 $^2\mu\text{m}^2$, 50 $^2\mu\text{m}^2$, 100 $^2\mu\text{m}^2$
CPG Edge Region Width	1 μm
Detector Type	p $^+$ -FD/n-body photogate
Diode Capacitance	\approx 250fF (50 μm^2 CPG)
Poly-Si Absorption (Sim'ed)	65% at 450nm ($\alpha=3.56\mu\text{m}^{-1}$) 30% at 520nm ($\alpha=1.35\mu\text{m}^{-1}$) 15% at 620nm ($\alpha=0.45\mu\text{m}^{-1}$)
Peak SNR (at 1500 $\mu\text{W}/\text{cm}^2$)	34.7dB at 450nm 29.2dB at 520nm 34.8dB at 620nm
Peak Responsivity	0.34, at 570nm (20 μm^2 CPG) 0.30, at 570nm (50 μm^2 CPG) 0.28, at 570nm (100 μm^2 CPG)

To ameliorate the scattering effects caused by uneven drying of QDs spotted on a surface, the QDs are imaged in the solution phase using a reservoir made from polydimethylsiloxane (PDMS) and glass. For tighter control of the geometry of the QD solution to be sensed, a reservoir is fabricated to contain the solution instead of depositing the QD on a sensing surface, such as a transparent cover slip on the CMOS imager.

To fabricate the reservoir, a cylindrical volume is removed by a metal punch from the PDMS, which is subsequently plasma bonded to a glass cover slip. The dimensions of the cover slips, which forms the bottom of the reservoir, are 22 mm (length) \times 22 mm (width) \times 150 μm (thick). The bottom of the reservoir is made as thin as possible to minimize the distance between the sample and the focal plane. The 4 mm-diameter reservoir with a side wall height of 1 mm holds a volume of 10 μL .

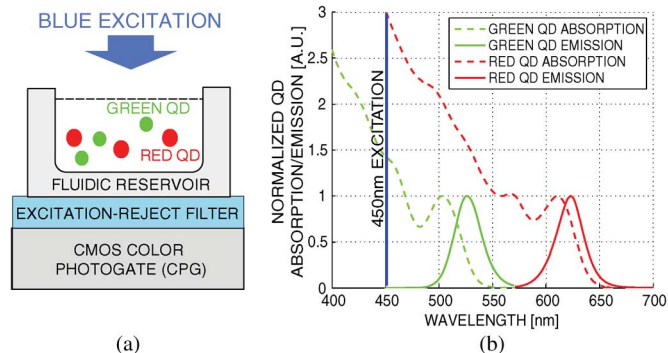


Fig. 13. (a) Application of CPG in a fluorescence detection microsystem (QD = Quantum Dot). (b) Fluorescence absorption and emission spectra of quantum dots.

B. Sample Preparation

Oleic acid capped organic core/shell CdSeS/ZnS based QDs from Cytodiagnostics have been made water-soluble by a ligand exchange reaction with 3-mercaptopropionic acid [35]. The quantum yields of the mercaptopropionic acid capped gQDs and rQDs are $0.19(\pm 0.02)$ and $0.25(\pm 0.03)$, respectively. As depicted in Fig. 13(b), the peak emission of gQDs and rQDs are at 527 nm and 623 nm, respectively, with a FWHM of 29 nm for both colors of QDs. The molar extinction coefficients are $411400 \text{ M}^{-1}\text{cm}^{-1}$ and $350000 \text{ M}^{-1}\text{cm}^{-1}$ for gQDs and rQDs, respectively.

C. Single-Color Quantum Dot Sensing

The fluorescence detection capability of the microsystem has been tested by measuring the emission intensity from various

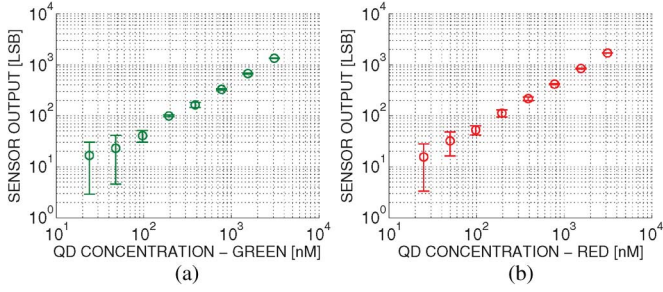


Fig. 14. Background-subtracted calibration curves obtained from single-color measurements of (a) gQDs, and (b) rQDs.

concentrations of gQDs and rQDs separately. Since the emission wavelength to be sensed is known when only one color of QD is present in the solution (i.e., 527 nm for gQD or 623 nm for rQD, but not both), emission intensity is the only quantity to be measured. As a result, for single-color experiments, the CPG functions as a regular non-spectral sensor, i.e., reconstruction using the color model is not necessary.

The calibration curves for rQDs and gQDs are depicted in Fig. 14(a) and (b), respectively. Each curve involves the detection of binary-weighted QD concentrations from $3 \mu\text{M}$ down to 24 nM, in eight concentration steps. Each error bar denotes one standard deviation from four measurements. Error bars are symmetrical on a linear scale and are included for all data points but in some cases are too small to be visible on the logarithmic plot. The higher response from the detector in case of rQDs as compared to gQDs is due to a higher molar absorptivity coefficient of rQDs as compared to gQDs at the 450 nm excitation wavelength [see excitation spectra of rQDs and gQDs in Fig. 13(b)].

To determine the detection limit, the noise statistics of the background are first measured. To account for the optical characteristics of the PDMS-glass structure, an empty reservoir filled with a 50 mM borate buffer (pH 9.25) solution is utilized in the measurement of the background signal. The mean and standard deviation of the background signal are 50 and 3.4 sensor output codes or LSBs, respectively, from 32 measurements. For each calibration curve, the background, which is attributed mainly to scattering of the excitation light, is subtracted from the measurements to determine the QD emission signal. For chemical measurements, the detection limit is conventionally defined as three standard deviations (3σ) above the mean of the background signal. In this case, $3\sigma = 10.2$ sensor output codes, which translates to a detection limit of approximately 24 nM for both colors of QDs, with a sample volume of $10 \mu\text{L}$.

D. Simultaneous 2-Color Quantum Dot Sensing

As discussed previously, the need for spatial registration for multiplexed detection can be avoided by means of spectral multiplexing, which is based on the detection of multiple emission wavelengths. In order to evaluate and demonstrate the multi-color detection capability of this microsystem, measurements of gQD and rQD concentrations in solutions contains both QDs have been performed.

Green QDs and red QDs are first prepared into four concentrations of 0 nM, 375 nM, 750 nM, or 1500 nM. The QDs are then mixed to form 16 solutions with unique ratios of gQD/rQD concentrations. Fig. 15 depicts measurements of gQD and rQD concentrations through the sensing of green and red fluorescence emissions from the 16 solutions. For example, solution S7 contains 750 nM and 375 nM of gQD and rQD, respectively.

The process of spectral sensing of QD emission is similar to that of the LED color light measurements. To invoke the spectral sensing capability of the CPG, the input is sampled at multiple CPG gate voltages. In this case of detecting two colors, two gate voltages are used ($V_{GB1} = 0 \text{ V}$, $V_{GB2} = 0.6 \text{ V}$, for V_{BODY} at 1.5 V). To improve detection accuracy, eight photocurrent measurements are performed at each V_{GB} . The measurements are then averaged and background subtracted. The set of two resulting averages at V_{GB1} and V_{GB2} then enter the reconstruction algorithm to obtain the green and red intensities, which correspond to the gQD and rQD concentrations. This process of measurement and reconstruction is repeated four times to obtain the error bars depicted in Fig. 15.

It can be observed from Fig. 15 that the standard deviations of the background signals at zero input concentrations are $\sigma_g \approx 40 \text{ nM}$ and $\sigma_r \approx 30 \text{ nM}$ for gQD and rQD, respectively. Based on the 3σ definition, the detection limits of 120 nM and 90 nM are achieved for gQD and rQD, respectively. Since $10 \mu\text{L}$ of sample volume is used for each measurement with detection limits in terms of concentration at 120 nM and 90 nM, the microsystem is able to detect 1.2 pmol and 0.9 pmol of gQD and rQD, respectively.

Larger error bars are observed in the quantum dot concentration measurements (Fig. 15) compared to the LED color light measurements (Fig. 12). This can largely be attributed to two main reasons. First, the test environment of LED illumination tests is much more stable in that the LED intensities are well controlled and the path on which light travels from the LED to the sensor is enclosed to suppress the influence of stray light. In contrast, although chemical laboratory techniques has been strictly followed, there is inevitably variation in the sample preparation. For example, although accurate micro-pipetting techniques has been used, the dilution of QDs into different concentrations introduces error. Second, as the excitation light reaches the uneven surface and the non-homogeneity of the QD sample solution, scattering occurs. Scattering characteristics are dependent on the geometry of the sample solution, which although mitigated by the use of the fluidic reservoir, cannot be completely eliminated.

VII. DISCUSSION

Table II compares the proposed sensor to CMOS filterless color sensors reported in the last five years. It is evident that the most popular topologies are the buried double and triple junctions [17], [18], [20]–[22]. A wide variety of CMOS process nodes have been used, with the latest development in a $0.11 \mu\text{m}$ technology [22]. Also, various readout techniques have been employed such as time division multiplexing [22], event-based readout [17], [18], and current readout [20], for applications ranging from biology to machine vision. For a comprehensive

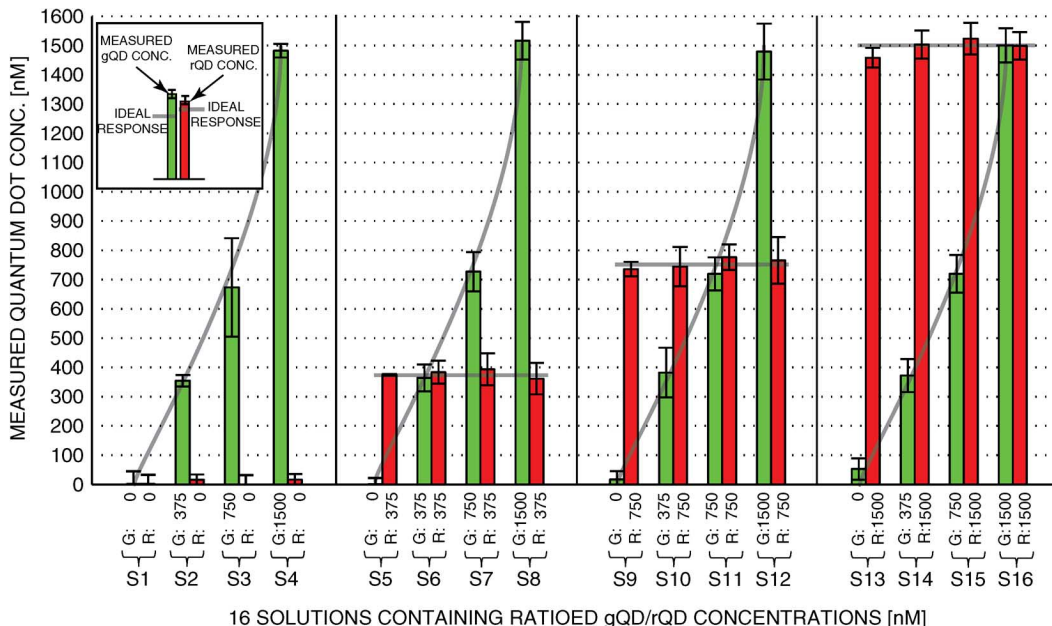


Fig. 15. Measurements of gQD and rQD concentrations by sensing of green and red fluorescence emission. Results from 16 solutions containing both gQD and rQD are plotted. For example, solution S7 contains 750 nM and 375 nM of gQD and rQD, respectively. Error bars are from four measurements and denote one standard deviation.

TABLE II
CMOS FILTERLESS COLOR SENSOR COMPARATIVE ANALYSIS

	This Work	[22]	[17]	[18]	[21]	[20]
Publication Year	2013	2012	2010	2010	2009	2007
CMOS Technology	0.35 μm	0.11 μm	0.18 μm	0.5 μm	1.5 μm	0.18 μm
Supply Voltage	3.3V	3.3V	1.8V	5V	5V	1.8V
Photodetector Type	p ⁺ /NW PGate	BTJ	BDJ	BDJ	BDJ	BTJ
Detector Size	20 ² ,50 ² ,100 ² μm^2	49.2 μm^2	144 μm^2	690 μm^2	160 \times 160 μm^2	N/A
Readout Type	<i>I</i> -to- <i>f</i>	TDM	Event-based	Event-based	Diff. Amp.	Current
On-chip ADC	YES	YES	YES	YES	NO	NO
Application	Fluorescence	Color / Depth	Color DVS	Color DVS	Retina	Skin Detection

BDJ = Buried Double Junction, BTJ = Buried Triple Junction, DVS = Dynamic Vision Sensor, TDM = Time Division Multiplexing

evaluation of the proposed CPG prototype, additional discussions are provided below.

As evident from (3) and (4), the CPG response has been modeled with a linear system. Based on Fig. 12, good linearity has been experimentally validated up to the light intensity of 1500 $\mu\text{W}/\text{cm}^2$. To further study linearity, a quadratic model (not reported in this work) has been investigated, such that (3) expands to

$$I'_1 = k_{11}\phi_1 + k_{12}\phi_2 + k'_{11}\phi_1^2 + k'_{13}\phi_2^2 \quad (17)$$

where k'_{11} and k'_{13} model the nonlinear components, for example, due to nonlinear effects in carrier collection. It is found that the k' -coefficients are of negligible values for the tested illumination range, which further suggests that nonlinearity is not significant. In the case where the CPG were to operate in a nonlinear range, for example when subjected to very high light input intensities beyond the level typically required for biolog-

ical applications, two approaches can be used. First, as suggested above, a higher order model can be used where the k -coefficient matrix is expanded to include nonlinear terms. Second, well-adopted modeling techniques such as binning [36] can be used, where the input space is subdivided into multiple regions such that different local k -coefficients can be assigned to particular input ranges for an accurate reconstruction.

As with most sensors, the CPG response is susceptible to process variations. However, it is worth noting that, since the k -coefficients are obtained empirically, process variation can largely be accounted for as it is embedded in the k -coefficients. For example, inter-die variations can be mitigated by using die-specific k -coefficients.

CMOS optical sensor detection limits can be improved by employing low-light techniques, for example, to reduce dark current [37] or using a dedicated capacitive transimpedance amplifier (CTIA) implemented in the pixel to integrate the photocurrent onto a small capacitor, rather than the photodiode par-

asitic capacitance [33]. However, these techniques tend to reduce fill factor and increase power consumption.

There are two main sources of error associated with the CPG sensor: the error introduced by the readout circuits and the error resulting from the reconstruction process. For the readout circuits, accuracy is limited by the temporal and fixed pattern noise (FPN) of the imager pixel and ADC. The ADC temporal noise can be improved by low-noise analog circuits or by system-level techniques such as oversampling [38], both at the expense of higher power consumption. FPN can be mitigated by, for example, calibrating for transistor threshold voltage variations [39]. To suppress the effect of temporal noise, multiple sampling has been found to be effective both in model generation and in the actual measurement of samples. To improve detection accuracy, averaging has been utilized in measurements involving chemical samples.

Measurement error is also affected by the properties of the reconstruction algorithm. For further investigation, a sensitivity analysis for the system of equations $\mathbf{I} = \mathbf{k}\mathbf{x}$ can be performed to determine the way in which the accuracy of the solution \mathbf{x} is affected by the accuracy of \mathbf{I} , where \mathbf{I} is the set of measurements from the sensor. It is worthy to note that this sensitivity is a property of the k -coefficient matrix and is determined by the responsiveness of the CPG across wavelengths and gate voltages.

VIII. CONCLUSION

A CMOS tunable-wavelength multi-color photogate sensor is presented. The CPG employs a polysilicon gate available in a standard CMOS process as an optical filter, thus requiring no external color filter. When applied to fluorescence-based biochemical detection microsystems, the CPG can be utilized to detect and differentiate among the emissions of green-emitting and red-emitting quantum dots at the nano-molar concentration level. The entire detection system utilizes only one long-pass optical filter for excitation attenuation, rather than color differentiation. The CPG has been experimentally validated by simultaneously sensing two colors of QDs, verifying its suitability for spectrally-multiplexed concentration measurements of biological analytes. The prototype demonstrates technologies that enable miniaturized, low-cost screening tools for medical diagnostics applications.

ACKNOWLEDGMENT

The authors thank Dr. Emanuel Istrate, Dr. Venkat Venkataraman, and Dr. Wai Tung Ng at the University of Toronto, for insightful technical discussions. The authors also thank Canadian Microelectronics Corporation (CMC) and the Natural Sciences and Engineering Research Council of Canada (NSERC) for prototype fabrication and funding.

REFERENCES

- [1] H. Eltoukhy, K. Salama, and A. Gamal, "A 0.18- μm CMOS bioluminescence detection lab-on-chip," *IEEE J. Solid-State Circuits*, vol. 41, no. 3, pp. 651–662, Mar. 2006.
- [2] M. Noor and U. Krull, "Microfluidics for the deposition of density gradients of immobilized oligonucleotide probes; Developing surfaces that offer spatial control of the stringency of DNA hybridization," *Anal. Chim. Acta.*, vol. 708, no. 1–2, pp. 1–10, Dec. 2011.
- [3] X. Gao, Y. Cui, R. Levenson, L. Chung, and S. Nie, "In vivo cancer targeting and imaging with semiconductor quantum dots," *Nature Biotechnol.*, vol. 22, no. 8, pp. 970–976, 2004.
- [4] O. Tigli, L. Bivona, P. Berg, and M. Zaghloul, "Fabrication and characterization of a surface-acoustic-wave biosensor in CMOS technology for cancer biomarker detection," *IEEE Trans. Biomed. Circuits Syst.*, vol. 4, no. 1, pp. 62–73, Feb. 2010.
- [5] R. Singh, D. Ho, A. Nilchi, G. Gulak, P. Yau, and R. Genov, "A CMOS/Thin-film fluorescence contact imaging microsystem for DNA analysis," *IEEE Trans. Circuits Syst. I, Reg. Papers*, vol. 57, no. 5, pp. 1029–1038, May 2010.
- [6] M. Schena, D. Shalon, R. Davis, and P. Brown, "Quantitative monitoring of gene expression patterns with a complementary DNA microarray," *Science*, vol. 270, no. 5235, pp. 467–470, Oct. 1995.
- [7] W. Algar and U. Krull, "Developing mixed films of immobilized oligonucleotides and quantum dots for the multiplexed detection of nucleic acid hybridization using a combination of fluorescence resonance energy transfer and direct excitation of fluorescence," *Langmuir*, vol. 26, no. 8, pp. 6041–6047, Apr. 2010.
- [8] M. Bruchez, M. Moronne, P. Gin, S. Weiss, and A. Alivisatos, "Semiconductor nanocrystals as fluorescent biological labels," *Science*, vol. 281, no. 5385, pp. 2013–2016, 1998.
- [9] D. Figeys and D. Pinto, "Lab-on-a-Chip: A revolution in biological and medical sciences," *Anal. Chem.*, vol. 72, no. 9, pp. 330–335, May 2000.
- [10] B. Kuswandi, Nuriman, J. Huskens, and W. Verboom, "Optical sensing systems for microfluidic devices: A review," *Anal. Chim. Acta.*, vol. 601, no. 2, pp. 141–155, Oct. 2007.
- [11] R. Mazurczyka, J. Vieillarda, A. Bouchardb, B. Hannesa, and S. Krawczyka, "A novel concept of the integrated fluorescence detection system and its application in a lab-on-a-chip microdevice," *Sens. Actuators B, Chem.*, vol. 118, no. 1–2, pp. 11–19, Oct. 2006.
- [12] X. Fang, V. Hsiao, V. Chodavarapu, A. Titus, and A. Cartwright, "Colorimetric porous photonic bandgap sensors with integrated CMOS color detectors," *IEEE Sensors J.*, vol. 6, no. 3, pp. 661–667, Jun. 2006.
- [13] Y. Maruyama, K. Sawada, H. Takao, and M. Ishida, "A novel filterless fluorescence detection sensor for DNA analysis," *IEEE Trans. Electron Devices*, vol. 53, no. 3, pp. 553–558, Mar. 2006.
- [14] A. Tavares, M. Noor, C. Vannoy, W. Algar, and U. Krull, "On-chip transduction of nucleic acid hybridization using spatial profiles of immobilized quantum dots and fluorescence resonance energy transfer," *Anal. Chem.*, vol. 84, no. 1, pp. 312–319, Jan. 2012.
- [15] S. Kong, D. Wijngaards, and R. Wolffenbuttel, "Infrared micro-spectrometer based on a diffraction grating," *Sens. Actuators A, Phys.*, no. 92, pp. 88–95, 2001.
- [16] J. Correia, G. Graaf, M. Bartek, and R. Wolffenbuttel, "A single-chip CMOS optical microspectrometer with light-to-frequency converter and bus interface," *IEEE J. Solid-State Circuits*, vol. 37, no. 10, pp. 1344–1347, Oct. 2002.
- [17] R. Berner and T. Delbruck, "Event-based pixel sensitive to change of color and brightness," *IEEE Trans. Circuits Syst. I, Reg. Papers*, vol. 58, no. 7, pp. 1581–1590, Jul. 2010.
- [18] R. Berner and T. Delbruck, "Event-based color change pixel in standard CMOS," in *Proc. IEEE Int. Symp. Circuits and Systems*, May 2010, pp. 349–352.
- [19] D. Fasnacht and T. Delbruck, "Dichromatic spectral measurement circuit in vanilla CMOS," in *Proc. IEEE Int. Symp. Circuits and Systems*, May 2007, pp. 3091–3094.
- [20] X. Zhao, F. Boussaid, and A. Bermak, "Characterization of a 0.18 μm CMOS color processing scheme for skin detection," *IEEE Sensors J.*, vol. 7, no. 11, pp. 1471–1474, Nov. 2007.
- [21] Z. Fu and A. Titus, "CMOS neuromorphic optical sensor chip with color change-intensity change disambiguation (CCICD)," *IEEE Sensors J.*, vol. 9, no. 6, pp. 689–696, Jun. 2009.
- [22] S. Kim, J. Kim, B. Kang, and L. K., "A CMOS image sensor based on unified pixel architecture with time-division multiplexing scheme for color and depth imaging acquisition," *IEEE J. Solid-State Circuits*, vol. 47, no. 11, pp. 2834–2845, Nov. 2012.
- [23] H. Ishii, Y. Maruyama, H. Takao, M. Ishida, and K. Sawada, "Improvement in filter-less fluorescence sensor capability by optimization of potential distribution," in *Proc. 4th Asia-Pacific Conf. Transducers and Micro-Nano Tech.*, Jun. 2008, pp. 68–71.
- [24] N. Nelson, D. Sander, M. Dandin, S. Prakash, A. Sarje, and P. Abshire, "Handheld fluorimeters for lab-on-a-chip applications," *IEEE Trans. Biomed. Circuits Syst.*, vol. 3, no. 2, pp. 97–107, Apr. 2009.

- [25] T. Huang, S. Sorgenfrei, P. Gong, R. Levicky, and K. Shepard, "A 0.18- μm CMOS array sensor for integrated time-resolved fluorescence detection," *IEEE J. Solid-State Circuits*, vol. 44, no. 5, pp. 1644–1654, May 2009.
- [26] S. Mendis, S. Kemeny, R. Gee, B. Pain, C. Staller, Q. Kim, and E. Fossum, "CMOS active pixel image sensors for highly integrated imaging systems," *IEEE J. Solid-State Circuits*, vol. 32, no. 2, pp. 187–197, Feb. 1997.
- [27] D. Ho, G. Gulak, and R. Genov, "CMOS field-modulated color sensor," in *Proc. IEEE Custom Integrated Circuit Conf.*, Sep. 2011.
- [28] S. Dimitrijević, *Principles of Semiconductor Devices*, 1st ed. London, U.K.: Oxford Univ. Press, 2006.
- [29] H. Wong, "Technology and device scaling considerations for CMOS imagers," *IEEE Trans. Electron Devices*, vol. 43, no. 12, pp. 2131–2142, Dec. 1996.
- [30] W. Lane and G. Wrixon, "The design of thin-film polysilicon resistors for analog IC applications," *IEEE Trans. Electron Devices*, vol. 36, no. 4, pp. 738–744, Apr. 1989.
- [31] R. Murali and J. Meindl, "Modeling the effect of source/drain junction depth on bulk-MOSFET scaling," *Solid State Electron.*, vol. 51, pp. 823–827, May 2007.
- [32] Z. Q. Li and Z. M. Li, "Comprehensive modeling of superluminescent light-emitting diodes," *IEEE J. Quantum Electron.*, vol. 46, no. 4, pp. 454–461, Apr. 2010.
- [33] K. Murari, R. Cummings, N. Thakor, and G. Gauwenberghs, "A CMOS in-pixel CTIA high-sensitivity fluorescence imager," *IEEE Trans. Biomed. Circuits Syst.*, vol. 5, no. 5, pp. 449–458, Oct. 2011.
- [34] K. Loo, Y. Lai, S. Tan, and C. Tse, "On the color stability of phosphor-converted white LEDs under DC, PWM, and bilevel drive," *IEEE Trans. Power Electron.*, vol. 27, no. 2, pp. 974–984, Feb. 2012.
- [35] A. Tavares, M. Noor, W. Algar, C. Vannoy, L. , and U. Krull, "Toward an on-chip multiplexed nucleic acid hybridization assay using immobilized quantum dot-oligonucleotide conjugates and fluorescence resonance energy transfer," *Proc. SPIE, Colloidal Quantum Dots/Nanocrystals for Biomedical Applications*, vol. 7909, no. 79090X, Jan 2011.
- [36] P. Li, "An adaptive binning color model for mean shift tracking," *IEEE Trans. Circuits Syst. Video Technol.*, vol. 18, no. 9, pp. 1293–1299, Sep. 2008.
- [37] R. Yotter and D. Wilson, "A review of photodetectors for sensing light-emitting reporters in biological systems," *IEEE Sensors J.*, vol. 3, no. 3, pp. 288–303, Jun. 2003.
- [38] Y. Matsuya, K. Uchimura, A. Iwata, T. Kobayashi, M. Ishikawa, and T. Yoshitome, "A 16-bit oversampling A-to-D conversion technology using triple-integration noise shaping," *IEEE J. Solid-State Circuits*, vol. 22, no. 6, pp. 921–929, Dec. 1987.
- [39] S. Kavadias, B. Dierickx, D. Scheffer, A. Alaerts, D. Uwaerts, and J. Bogaerts, "A logarithmic response CMOS image sensor with on-chip calibration," *IEEE J. Solid-State Circuits*, vol. 35, no. 8, pp. 1146–1152, Aug. 2000.



Derek Ho (S'09) received the B.A.Sc. (first class) and M.S. degrees from the University of British Columbia, Vancouver, BC, Canada, in 2005 and 2007, respectively.

Currently, he is working toward the Ph.D. degree in the Department of Electrical and Computer Engineering, University of Toronto, Toronto, ON, Canada. His research interests are in mixed-signal VLSI circuits and systems for sensory acquisition and processing with emphasis on spectral and wide-dynamic range imaging, photonic lab-on-a-chip, point-of-care screening, and biochemical detection applications.

Mr. Ho was the recipient of the Postgraduate Scholarship and Undergraduate Student Research Award from the Natural Sciences and Engineering Research Council of Canada. He was also awarded the Ontario Graduate Scholarship in Science and Technology, and the Mary H. Beatty Fellowship.



M. Omair Noor received the Hon. B.Sc. degree in the biotechnology specialist program and the M.Sc. degree in bioanalytical chemistry from the University of Toronto Mississauga, Mississauga, ON, Canada, in 2008 and 2010, respectively.

Currently, he is working toward the Ph.D. degree in the Department of Chemistry at the University of Toronto, Toronto, ON, Canada, with the Chemical Sensors Group under the supervision of Prof. Ulrich J. Krull. His research interests focus on the integration of quantum dots and FRET based assays for nucleic acid detection using microfluidic channels and paper as solid supports.

Mr. Noor holds an Ontario Graduate Scholarship (OGS) from the Ontario Ministry of Training, Colleges and Universities (MTCU). He was also awarded the Undergraduate Student Research Award (USRA) from the Natural Sciences and Engineering Research Council of Canada (NSERC).



Ulrich J. Krull is appointed as a Professor of Analytical Chemistry at the University of Toronto, Toronto, ON, Canada, and holds the endowed AstraZeneca Chair in Biotechnology.

His research interests are in the areas of biosensor and diagnostic technologies, and applications to biotechnology, forensic, clinical and environmental chemistry. His research work is exploring the use of nanoscale materials and microfluidics technologies to build devices for detection of DNA and RNA targets. Prof. Krull is an editor for *Analytica Chimica Acta*, and serves on a number of scientific advisory boards for industry.



Glenn Gulak (M'90–SM'96) received the Ph.D. degree from the University of Manitoba, Winnipeg, MB, Canada, while holding a Natural Sciences and Engineering Research Council of Canada Postgraduate Scholarship.

He is a Professor in the Department of Electrical and Computer Engineering at the University of Toronto, Toronto, ON, Canada. He is a registered Professional Engineer in the Province of Ontario. His present research interests are in the areas of algorithms, circuits, and CMOS system-on-chip implementations for digital communication systems and, additionally, in the area of CMOS biosensors. His current research projects are focused on high-performance MIMO OFDM implementations and in CMOS biosensors. He has authored or coauthored more than 100 publications in refereed journal and refereed conference proceedings. He has received numerous teaching awards for undergraduate courses taught in both the Department of Computer Science and the Department of Electrical and Computer Engineering at the University of Toronto. He held the L. Lau Chair in Electrical and Computer Engineering for the 5-year term from 1999 to 2004. From March 2001 to March 2003 he was the Chief Technical Officer and Senior VP LSI Engineering of a fabless semiconductor startup headquartered in Irvine, CA, USA. From January 1985 to January 1988 he was a Research Associate in the Information Systems Laboratory and the Computer Systems Laboratory at Stanford University, Stanford, CA, USA. He holds the Canada Research Chair in Signal Processing Systems and the Edward S. Rogers Sr. Chair in Electrical Engineering.

Dr. Gulak has served on the ISSCC Signal Processing Technical Subcommittee from 1990 to 1999, ISSCC Technical Vice-Chair in 2000 and served as the Technical Program Chair for ISSCC 2001. He received the IEEE Millennium Medal in 2001. He served on the Technology Directions Subcommittee for ISSCC from 2005 to 2008. He currently serves as the Chair of the Publications Committee for the IEEE Solid-State Circuits Society.



Roman Genov (S'96–M'02–SM'11) received the B.S. degree in electrical engineering from the Rochester Institute of Technology, Rochester, NY, USA, in 1996, and the M.S.E. and Ph.D. degrees in electrical and computer engineering from The Johns Hopkins University, Baltimore, MD, USA, in 1998 and 2002, respectively.

He has held engineering positions at Atmel Corporation, Columbia, MD, USA, in 1995 and Xerox Corporation, Rochester, NY, USA, in 1996. He was a Visiting Researcher in the Laboratory of Intelligent Systems at the Swiss Federal Institute of Technology (EPFL), Lausanne, Switzerland, in 1998 and in the Center for Biological and Computational Learning at the Massachusetts Institute of Technology, Cambridge, MA, USA, in 1999. He is currently an Associate Professor in the Department of Electrical and Computer Engineering, University of Toronto, Toronto, ON, Canada. His research interests include analog and digital VLSI circuits, systems and algorithms for

energy-efficient signal processing with applications to electrical, chemical and photonic sensory information acquisition, biosensor arrays, brain-silicon interfaces, parallel signal processing, adaptive computing for pattern recognition, and implantable and wearable biomedical electronics.

Dr. Genov is a corecipient of Best Paper Award of the IEEE Biomedical Circuits and Systems Conference, Best Student Paper Award of the IEEE International Symposium on Circuits and Systems, Best Paper Award of the IEEE Circuits and Systems Society Sensory Systems Technical Committee, Brian L. Barge Award for Excellence in Microsystems Integration, MEMSCAP Microsystems Design Award, the DALSA Corporation Award for Excellence in Microsystems Innovation, and the Canadian Institutes of Health Research Next Generation Award. He was a Technical Program Co-Chair at the IEEE Biomedical Circuits and Systems Conference. He was an Associate Editor of IEEE TRANSACTIONS ON CIRCUITS AND SYSTEMS II: EXPRESS BRIEFS and *IEEE Signal Processing Letters*. He is currently an Associate Editor of IEEE TRANSACTIONS ON BIOMEDICAL CIRCUITS AND SYSTEMS.